

JGR Space Physics

RESEARCH ARTICLE

10.1029/2022JA031155

Key Points:

- This paper provides a list of the Jovian magnetosphere boundary crossings by the Juno spacecraft from June 2016 to August 2022
- Jovian magnetospheric compressions lead to increased bKOM radio emissions (immediately) and DAM on the dusk sector (more than one rotation later)
- nKOM radio emission appears later during relaxation phase of the compression

Supporting Information:

Supporting Information may be found in the online version of this article.

Correspondence to:









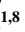







C. K. Louis,
corentin.louis@obspm.fr

Citation:

Louis, C. K., Jackman, C. M., Hospodarsky, G., O’Kane Hackett, A., Devon-Hurley, E., Zarka, P., et al. (2023). Effect of a magnetospheric compression on Jovian radio emissions: In situ case study using Juno data. *Journal of Geophysical Research: Space Physics*, 128, e2022JA031155. <https://doi.org/10.1029/2022JA031155>

Received 6 DEC 2022
Accepted 18 AUG 2023

Effect of a Magnetospheric Compression on Jovian Radio Emissions: In Situ Case Study Using Juno Data

C. K. Louis^{1,2,3} , C. M. Jackman¹ , G. Hospodarsky⁴ , A. O’Kane Hackett^{1,5} , E. Devon-Hurley^{1,5} , P. Zarka^{2,3} , W. S. Kurth⁴ , R. W. Ebert^{6,7} , D. M. Weigt^{1,8} , A. R. Fogg¹ , J. E. Waters⁹ , S. C. McEntee^{1,5} , J. E. P. Connerney¹⁰ , P. Louarn¹¹ , S. Levin¹² , and S. J. Bolton⁶ 

¹School of Cosmic Physics, DIAS Dunsink Observatory, Dublin Institute for Advanced Studies, Dublin, Ireland,

²Observatoire Radioastronomique de Nançay, Observatoire de Paris, Université PSL, CNRS, University Orléans, Nançay,

France, ³LESIA, Observatoire de Paris, PSL Research University, CNRS, Sorbonne Université, UPMC University Paris

06, University Paris Diderot, Meudon, France, ⁴Department of Physics and Astronomy, University of Iowa, Iowa City, IA,

USA, ⁵School of Physics, Trinity College Dublin, Dublin, Ireland, ⁶Southwest Research Institute, San Antonio, TX, USA,

⁷Department of Physics and Astronomy, University of Texas at San Antonio, San Antonio, TX, USA, ⁸Department of

Computer Science, Aalto University, Aalto, Finland, ⁹Department of Physics and Astronomy, University of Southampton,

Southampton, UK, ¹⁰Space Research Corporation, Annapolis, MD, USA, ¹¹IRAP, Université de Toulouse, CNRS, CNES,

UPS, Toulouse, France, ¹²Jet Propulsion Laboratory, Pasadena, CA, USA

Abstract During its polar orbits around Jupiter, Juno often crosses the boundaries of the Jovian magnetosphere (namely the magnetopause and bow shock). From the boundary locations, the upstream solar wind dynamic pressure can be inferred, which in turn illustrates the state of compression or relaxation of the system. The aim of this study is to examine Jovian radio emissions during magnetospheric compressions, in order to determine the relationship between the solar wind and Jovian radio emissions. In this paper, we give a complete list of bow shock and magnetopause crossings (from June 2016 to August 2022), and the associated solar wind dynamic pressure and standoff distances inferred from Joy et al. (2002, <https://doi.org/10.1029/2001JA009146>). We then select two sets of magnetopause crossings with moderate to strong compression of the magnetosphere for two case studies of the response of the Jovian radio emissions. We confirm that magnetospheric compressions lead to the activation of new radio sources. Newly activated broadband kilometric emissions are observed almost simultaneously with compression of the magnetosphere, with sources covering a large range of longitudes. Decametric emission sources are seen to be activated more than one rotation later only at specific longitudes and dusk local times. Finally, the activation of narrowband kilometric radiation is not observed until the magnetosphere is in its expansion phase.

1. Introduction

Planetary studies often face the challenge of interpreting in situ spacecraft observations without the benefit of an upstream monitor revealing the prevailing conditions in the interplanetary medium. This is particularly true of the outer planets. Radio emissions provide a direct probe of the site of particle acceleration and have potential to be used as a proxy for magnetospheric dynamics (see e.g., Cecconi et al. (2022) for Saturn; Fogg et al. (2022) for Earth). At Jupiter, the radio spectrum is composed of at least six components, from low-frequency emissions, such as quasi-periodic (QP) bursts or trapped continuum radiation (from a few kHz to 10s of kHz), up to decametric (DAM) emissions ranging from a few MHz to 40 MHz (Gurnett & Scarf, 1983; Louis et al., 2021a; Zarka, 1998).

In this study, we focus on three types of radio emissions observable with Juno: narrowband kilometric (nKOM), broadband kilometric (bKOM), and auroral DAM emissions (i.e., not induced by Galilean moons). The nKOM is attributed to a mode conversion mechanism producing emissions inside Io’s torus at or near the local electron plasma frequency (Barbosa, 1982; Gurnett & Scarf, 1983; Jones, 1988; Ronnmark, 1992). The last two components (bKOM and DAM) are auroral emissions, produced by the cyclotron maser instability (CMI), near the local electron cyclotron frequency. The sources of these emissions are located on magnetic field lines of magnetic apex (M-Shell) between 10 and 60 (unitless distance of the magnetic field line at the magnetic equator normalized to Jovian radius 71,492 km). These emissions are very anisotropic and beamed along the edges of a hollow cone

with an opening of $\sim 75^\circ \pm 5^\circ$ to $\sim 90^\circ$ with respect to the local magnetic field lines (Imai et al., 2019; Ladreiter et al., 1994; Louarn et al., 2017, 2018; Louis et al., 2019a; Treumann, 2006; Zarka, 1998).

The relation of the different components of Jupiter's radio emissions to both internal and external drivers is complex, as shown by several previous studies. These studies show a relationship between some of the components and external (solar wind) or internal (rotation, magnetic reconfiguration) drivers. Recently, Zarka et al. (2021) have reanalyzed data from Cassini's flyby of Jupiter, and found that hectometric (HOM) and DAM emissions are dominantly rotation-modulated (i.e., emitted from lighthouse-like sources fixed in Jovian longitude), whereas bKOM is modulated more strongly by the solar wind than by the rotation (i.e., emitted from sources more active within a given Local Time sector). This last study extends earlier results by Zarka and Genova (1983), Genova et al. (1987), and Imai et al. (2008, 2011). Louarn et al. (1998), using Galileo radio observations, have shown a sudden onset, and increased intensity (up to $2 \times 10^{-7} \text{ V m}^{-1} \text{ Hz}^{-1/2}$ at 5 MHz) of bKOM and DAM radio emissions, as well as the activation of new nKOM radio emissions, during periods of magnetospheric disturbance. They postulated large-scale energetic events as reconfigurations of the magnetosphere and plasma sheet somewhat analogous to terrestrial substorms. The results obtained by Echer et al. (2010), using Ulysses spacecraft data during the distant Jupiter encounter and Nançay Decameter Array (NDA) data, show that non-Io DAM radio emissions occur during intervals of enhanced solar wind dynamic pressure, but without any direct correlation between the emission duration or power versus the solar wind pressure or the interplanetary shock Mach number. Using 50 days of observations from Cassini and Galileo, Gurnett et al. (2002) showed that HOM emissions were triggered by the arrival of interplanetary shocks at Jupiter. Hess et al. (2012, 2014) have also shown that an increase of the solar wind pressure affects the non-Io-DAM radio emissions, using ground-based radio measurements (Hess et al., 2012) and Cassini and Galileo radio and magnetic measurements (Hess et al., 2014). These two studies have compared the type of shocks with the region of source activation. There are two types of shocks (Kilpua et al., 2015): fast forward shocks (FFSs) and fast reverse shocks (FRSs). These shocks are driven by solar coronal mass ejections (CME) or corotating interaction regions (CIR). The sudden explosion of a CME, at a higher velocity than the ambient solar wind, usually drives an FFS. As this fast CME expands into the solar system and overtakes the slower background solar wind, a compressed interaction region is usually formed, which is delimited by FFS on one side and FRS on the other side (Smith & Wolfe, 1976; Tsurutani et al., 2006). An FFS is characterized by a sharp or discontinuous increase of the solar wind velocity, density, temperature, and magnetic field amplitude. An FRS is characterized by an increase of the solar wind velocity, but a decrease of the solar wind temperature, density, and magnetic field amplitude. Both Hess et al. (2012, 2014) studies have shown that FFS trigger mostly dusk emissions, whereas FRS trigger both dawn and dusk emissions, with a time delay depending on the strength/direction of the interplanetary magnetic field (IMF). All the shock-triggered radio sources were found to subcorotate (i.e., rotating slower than the rotation period of Jupiter) with a rate ranging from 50% to 80% depending on the intensity of the IMF. These rates could, respectively, correspond to the extended and compressed states of the Jovian magnetosphere.

The above cited studies relied on sparse data sets (flybys or remote measurements) but the once-in-a-generation Juno data set gives the opportunity for longer-term monitoring of the Jovian system and its radio response. In particular, the apojoves early in the mission, which took Juno out to radial distances of $\sim 110 R_J$ on the dawn side, place the spacecraft near the nominal magnetopause and bow shock locations, and afford the opportunity to sample snippets of in situ solar wind, as well as to determine the positions of the magnetospheric boundaries at various points in time. All the while, the Juno radio instrument is constantly monitoring the Jovian radio spectrum. In this study, we utilize this unique data set to explore the connection between the solar wind and Jupiter's radio emissions by presenting the first case study of its kind.

Section 2 describes the data sets and processing methodology. Section 3 presents case studies of the Jovian radio emission response to two moderate to strong magnetospheric compressions inferred from multiple magnetopause crossings while Juno is on the outbound leg of its trajectory. Finally, in Section 4, we summarize and discuss the results of this study and present the perspectives.

2. Methodology

Since July 2016, Juno has been in orbit around Jupiter, making a polar orbit every 53 days during its prime mission. Since the Ganymede flyby in June 2021, the orbits have been shortened to 43 days, before being reduced to 38 days in September 2022 with the Europa flyby. During its first 44 orbits, with an apojove of up to $\sim 110 R_J$,

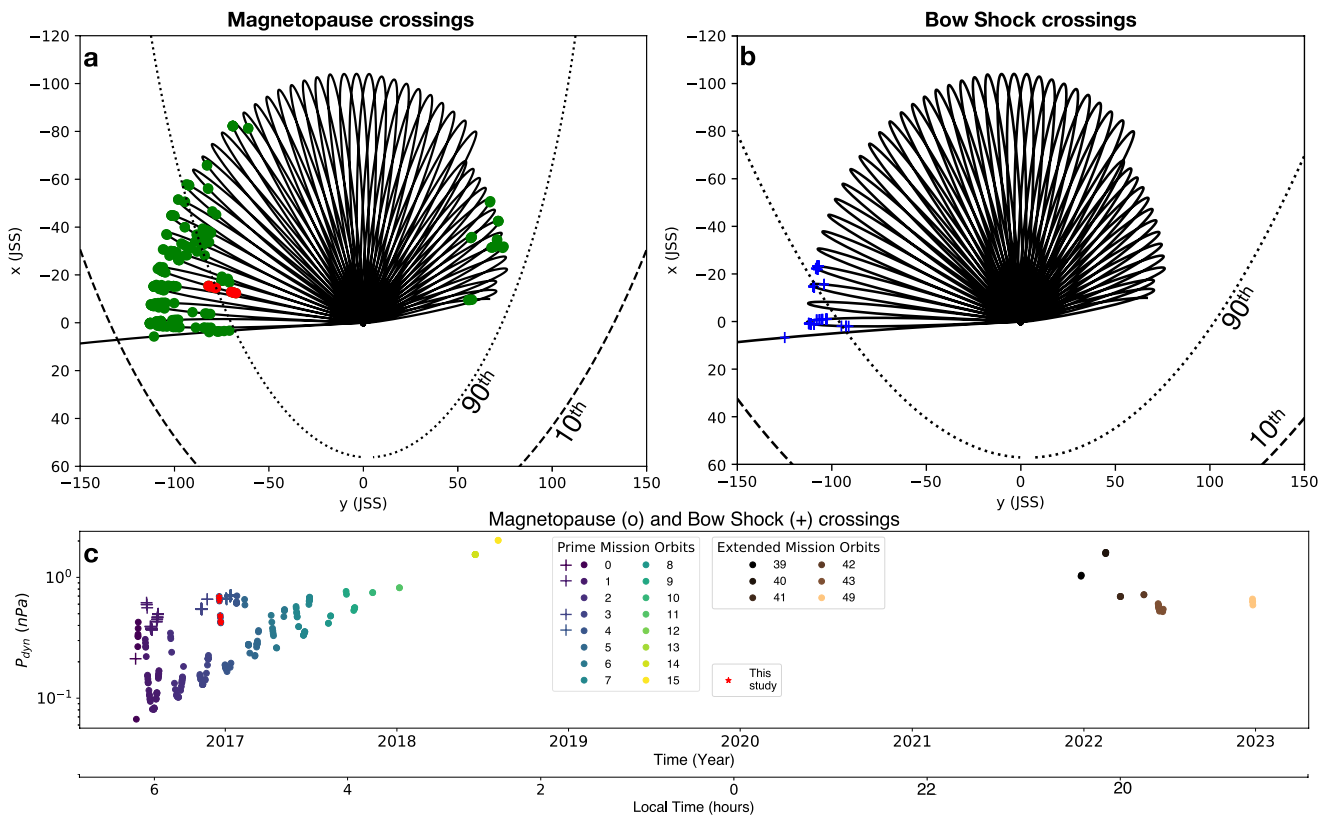


Figure 1. Projection of the Juno trajectory into the equatorial plane, with the (a) magnetopause and (b) bow shock crossings overplotted. The magnetopause crossings studied in this article are highlighted in red in panel (a). The coordinate system used here is the Jupiter-de-Spun-Sun (JSS). In this system, X points toward the Sun, Z is aligned with the Jovian spin axis, and Y closes the right-handed system (positive toward dusk). In panel (a), the dashed line represents the 10th quantile position of the magnetopause (0.03 nPa), the dotted line its 90th quantile position (0.518 nPa). In panel (b), these same lines represent the 10th (0.063 nPa) and 90th (0.579 nPa) quantile positions of the bow shock (values from Joy et al. (2002)). Panel (c) displays the solar wind dynamic pressure P_{dyn} values inferred from Joy et al. (2002), for each crossing (“+”: magnetopause; “o”: bow shock), as a function of time and Local Time (12:00: direction of the Sun; 00:00: opposition to the Sun). The color code corresponds to the orbit number. The cases studied in this article are highlighted in red.

Juno crossed the boundaries of the magnetosphere several times (Collier et al., 2020; Hospodarsky et al., 2017; Montgomery et al., 2022; Ranquist et al., 2019), as shown in Figure 1 projected into the equatorial plane. Figure 1a displays the magnetopause crossings while Figure 1b displays the bow shock crossings. In both of these panels are drawn the 10th and 90th quantile position of the magnetopause and bow shock, respectively, based on the Joy et al. (2002) model. Note that this model was built on crossings from Ulysses, Voyager, and Galileo, and thus may not be representative of all local times (especially the previously poorly explored dusk flank) or high-latitudes. The coordinate system used in this figure is the Juno-de-Spun-Sun (JSS), as this is the coordinate system used in the Joy et al. (2002) model. In this system, X points toward the Sun, Z is aligned with the Jovian spin axis, and Y closes the right-handed system (positive toward dusk). A 3D projection plot (in the Jupiter-Sun-Orbit (JSO) coordinate system) of the Jovian magnetosphere boundary crossings is shown in Figure S1 in Supporting Information S1. In the JSO system, X is aligned with the Jupiter-Sun vector, Y indicates the Sun's motion in Jupiter frame, and Z closes the system.

In this study, the boundary crossings displayed Figure 1 were determined using the radio measurements of the low-frequency receiver of the Juno/Waves instrument (Kurth et al., 2017), and the magnetic field measurements of the Juno/MAG instrument using the Fluxgate Magnetometer measurements (Connerney et al., 2017), following the work done by Hospodarsky et al. (2017). Three examples are shown in Figure 2, with Juno/Waves data (using Louis et al., 2021a, 2021b, estimated flux density data set) displayed in the top panels, and Juno/MAG data (in spherical JSO coordinates system) in the bottom panels. The “out” crossings (black-dashed lines) correspond to a boundary moving toward Jupiter, e.g., Figures 2a and 2d, Juno crosses the bow shock going from the magnetosheath to the solar wind. The “in” crossings (gray-shaded lines) define a boundary moving away from Jupiter, e.g., Juno crosses the bow shock, leaving the solar wind to enter the magnetosheath.

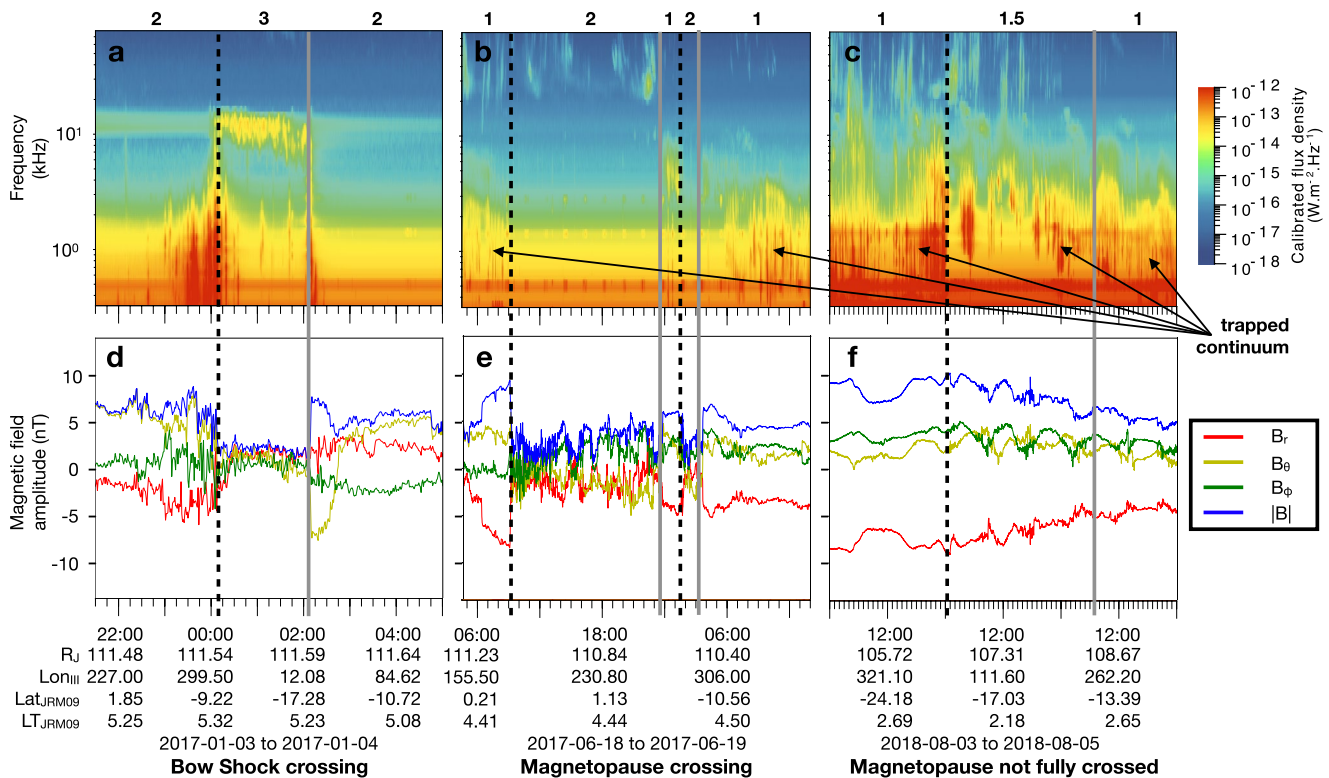


Figure 2. Examples of magnetospheric boundary crossings. Top panels (a)–(c) display Juno/Waves measurements (using Louis et al., 2021a, 2021b, estimated flux density data set), while bottom panels (d)–(f) display Juno/MAG measurements in spherical JSO coordinates. Outbound crossings (boundary moving toward Jupiter) are highlighted by the black-dashed lines, while inbound crossings (boundary moving away from Jupiter) are highlighted by the gray-shaded lines. (left (a, d)) Bow shock crossings; (middle (b, e)) magnetopause crossings; (right (c, f)) example where the Juno spacecraft partially crossed the magnetopause without ever actually passing from the magnetosphere to the magnetosheath (i.e., moved around the border). The numbers above the Waves data indicate the region where Juno is located: (1) magnetosphere, (2) magnetosheath, (3) solar wind, (1.5): “in” the magnetopause boundary.

The bow shock is a discontinuity formed when the supersonic solar wind is slowed to subsonic by interaction with the Jovian magnetic obstacle. A bow shock crossing is detected from the change in magnetic field amplitude and in the level of field fluctuations in the Juno/MAG data between the solar wind and the magnetosheath (Figure 2d). In the Juno/Waves measurements (Figure 2a) one can observe (a) an intense and broadband signal at the crossing and (b) Langmuir waves when Juno is inside the solar wind, visible here at ~ 10 kHz, which are produced by solar electrons reflected back into the solar wind from the shock boundary (Filbert & Kellogg, 1979; Scarf et al., 1971).

The position of the magnetopause is determined by the balance between the solar wind dynamic pressure and the plasma pressure in the outer magnetosphere (Mauk et al., 2004). A magnetopause crossing is detected by the appearance/disappearance in the Juno/Waves data (see Figure 2b) of the trapped continuum radiation, usually observed between 0.5 and 2 kHz. This signal is only seen when the observer is inside Jupiter's magnetosphere, in this example before the black-dashed line at ~ 18 June 2017 T09:00, and after the gray-shaded line at ~ 19 June 2017 T03:00. This trapped continuum radiation propagates at a frequency lower than the plasma frequency inside the magnetosheath and therefore cannot propagate into the magnetosheath (hence the name “trapped”). Juno/MAG measurements of the magnetic field amplitude (Figure 2e) also show a change as Juno crosses the magnetopause, passing from the magnetosphere into the magnetosheath (see, e.g., black-dashed line at ~ 18 June 2017 T09:00), with a decrease in magnetic field total amplitude $|B|$ and a much more disturbed signal than in the magnetosphere.

In some observations (see Figure 2c, between black-dashed and gray-shaded lines), low and high cut-off frequencies of the trapped continuum increase. Before ~ 04 August 2018 T00:00 (black-dashed line) and after ~ 05 August 2018 T07:00 (gray-shaded line), the trapped continuum radiation is visible between ~ 0.3 and ~ 4 kHz. In-between, the trapped continuum radiation is no longer visible at low frequency, but is shifted to higher

frequencies (between ~ 0.6 and ~ 8 kHz) and is very bursty. The high frequency part never completely disappears, and no drastic change in magnetic field components (Figure 2f) is observed, although they are more disturbed than in the magnetosphere, but less than in the magnetosheath. In the observation shown in Figures 2c and 2f, Juno is on the outbound part of its trajectory and is therefore moving away from Jupiter. We interpret these observations as the movement of the magnetopause toward Juno at first (increase of low and high cut-off frequencies, see black-dashed line). Subsequently, the magnetopause stops moving toward Jupiter, and Juno never completely crosses the magnetopause to end up in the magnetosheath (between black-dashed and gray-shaded lines). Juno is, however, close enough to the magnetopause, or even in the boundary layer (Went et al., 2011), to observe an increase of the low-frequency cut-off of the trapped continuum by the increasing density when approaching the boundary. Finally, the magnetopause is moving away from Jupiter (faster than Juno's velocity), and high and low cut-off frequencies decrease (Juno is again completely in the magnetosphere).

From the boundary positions, we can infer the solar wind dynamic pressure P_{dyn} using the Joy et al. (2002) model, by solving their second order polynomial equation (Equation 1 of Joy et al. (2002)). From this, we can determine if the crossings of the magnetospheric boundaries are due to compressions of the magnetosphere, by comparing the inferred P_{dyn} values to either Joy et al. (2002) quantile values, or observed solar wind P_{dyn} distributions upstream of Jupiter (Jackman & Arridge, 2011). One should note that the P_{dyn} value determined using Juno's position is not absolute, but a lower limit of the dynamic pressure. Although Juno is outbound, we cannot directly infer how far the magnetopause boundary is pushed back toward Jupiter.

Figure 1c displays the inferred P_{dyn} for all crossings (“+”: magnetopause; “o”: bow shock) as a function of time and Local Time. Note that there is a trend of increasing P_{dyn} values with time and decreasing Local Time. This is due to the procession of orbits, taking Juno more and more toward the night side of the magnetosphere (midnight Local Time), and thus deep into the magnetotail. This means that the magnetosphere has to be more compressed for Juno to cross the magnetospheric boundaries from this location. The bow shock is even further out again and thus Juno did not encounter the dawn side bow shock after the first few Juno orbits.

In the absence of an upstream monitor, we can compare these inferred P_{dyn} values with those provided by solar wind propagation models (e.g., Tao et al., 2005). For this, we must take into account any uncertainty on the propagation model values due to angle from opposition where predictions are most reliable. From this propagation model, we can also infer the type of shock (FFS or FRS) that compresses the magnetosphere as discussed in Section 1.

The full list of magnetopause and bow shock crossings (from 24 June 2016 to 26 July 2022, i.e., up to orbit 41) are available in Tables S1 and S2 in Supporting Information S1, along with the position of Juno (in cartesian JSS—mandatory to use Joy et al. (2002) model—and cartesian and spherical International Astronomical Union (IAU) System III (SIII) coordinates system), the inferred solar wind dynamic pressure and the position of the magnetosphere standoff distances (bow shock and magnetopause) inferred from the Joy et al. (2002) model (Louis et al., 2022a). Figure S2 in Supporting Information S1 displays statistical distributions based on the magnetosphere boundary crossings (Local Time, solar wind dynamic pressure, magnetopause, and bow shock positions).

We next investigate the response of bKOM and DAM emissions to magnetospheric compression in a case study. For that, we use the Louis et al. (2021a) data set (Louis et al., 2021b) and catalog of the radio emissions (Louis et al., 2021c). This catalog contains the Jovian radio emissions identified in the Juno/Waves observations, only from 09 April 2016 to 24 June 2019 (e.g., up to the 21st apojove of Juno). The radio components were visually identified according to their time-frequency morphology and then manually encircled by contours and labeled, using a dedicated program that records the coordinates of the contours and the label of each emission patch (Louis et al., 2022b, 2022c). While nKOM patches can be identified individually (fuzzy patches of emission elongated in time), the bKOM and DAM components have not been explicitly cataloged because they are the most frequent emissions in their respective frequency range. They can be selected and studied by excluding all other components and restricting to the adequate frequency range. For example, excluding nKOM in the range 20–140 kHz allows one to select the bKOM component only. In the [3.5–40.5] MHz frequency range, only decametric emissions induced by the Galilean moons Io, Europa, and Ganymede have been labeled (based on Louis et al. (2019b) simulations of those radio emissions, see Louis et al. (2020) for more details). Therefore, by excluding them, only auroral DAM emissions remain in this range. Given that HOM emissions can extend up to a few MHz, the highest part of the hectometric emission could be present in this range, but would only represent a minority of the emissions observed.

For the case studies described in Section 3, we decided to select the magnetopause crossings that took place between 19 December 2016 and 23 December 2016, highlighted in red in Figure 1. This choice is based on three factors: (a) in 2016–2017, the Jovian Auroral Distributions Experiment (JADE, McComas et al., 2017) was not activated during excursions into the solar wind, excluding in situ plasma information, and thus a direct measurement of P_{dyn} . Therefore, we decided to choose among one of the (more numerous) magnetopause crossing cases; (b) the case chosen had to be within the time interval covered by the catalog of Louis et al. (2021a, i.e., between 09 April 2016 and 24 June 2019); (c) in order to avoid any bias related to an extremely exceptional case, we did not select the case with the highest P_{dyn} value (second half of 2018, orbit 15).

The time interval chosen presents two main advantages. (a) There are two sets of crossings in a row. The P_{dyn} value determined for the first crossing (19 December 2016 T01:50) is 0.70 nPa. The dynamic pressure associated with the second set of crossings (21 December 2016 T08:48) is 0.48 nPa. The distribution of P_{dyn} at Jupiter published by Jackman and Arridge (2011, see their Figure 4b) reveals a peak at 0.05 nPa and a maximum slightly above 1 nPa. The 0.48 and 0.70 values therefore lie toward the tail of this distribution. Moreover, these inferred values are close to the 90th quantile value (0.518 nPa) of the magnetopause position given by Joy et al. (2002). Therefore, these two sets of magnetopause crossings correspond to a strong and a moderate compression. (b) Based on Figure 1c (red points) the P_{dyn} values associated with these magnetopause crossings are well above the “trend,” and therefore correspond to the strongest compressions during orbit 4. Recall that this “trend” is due to the procession of Juno's orbit, taking the spacecraft deep into the magnetotail, implying that the magnetosphere needs to be more compressed for Juno to cross the magnetospheric boundaries.

3. Jovian Auroral Radio Emission Response to Compressions of the Magnetosphere

3.1. Determination of the Compression

Figure 3 displays Juno measurements during magnetopause crossings for a 7-day interval from 17 December 2016 T00:00 to 24 December 2016 T04:15. Black-dashed lines show when Juno crossed the magnetopause from the magnetosphere to the magnetosheath (outbound crossings), while gray-shaded lines show inbound crossings. Figures 3a and 3b display Juno/Waves measurements for two different frequency ranges: (a) [3–40.5] MHz and (b) [0.3–140.0] kHz. Figure 3c displays Juno/MAG measurements: total amplitude $|B|$, and (r, θ, ϕ) components in JSO spherical coordinates system. The black line displays the Kivelson and Khurana (2002) and Khurana et al. (2004) magnetic field variation fit in the lobes (beyond $r = 30$ Jovian radii, the lobe magnetic field falls off as $B_{\text{lobe}}(\text{nT}) = (2.94 \pm 0.07) \times 10^3 r^{-1.37 \pm 0.01}$). Therefore, for an observer inside the magnetosphere, and if the magnetosphere is in a steady-state, $|B|$ should follow $|B_{\text{lobe}}|$. Figures 3d–3f display integrated time series of the radio signal measured by Juno/Waves for three different radio components: (d) auroral DAM (i.e., excluding the satellite-related DAM emissions), (e) bKOM, and (f) nKOM.

As described in Section 2 (see Figures 2b and 2e), the magnetopause crossings are clearly seen in Figure 3b from the disappearing of the trapped continuum radiation and in Figure 3c from the change in the magnetic field components and total amplitude (see the black-dashed and gray-shaded lines). Looking in more detail at Juno/MAG measurements (Figure 3c), one can notice at ~18 December 2016 T09:00 (indicated by the red dotted line), i.e., ~18 hr before the crossing of the magnetopause, an increase of the $|B|$ (blue curve) and B_ϕ (green curve) components while the B_r (red curve) and B_θ (yellow curve) components decrease. This is followed by turbulence observed in all magnetic field components, but without the sharp decrease in $|B|$ characteristic of magnetic measurements in the magnetosheath. We also see, approximately at the same time, that the cut-off frequencies of the trapped continuum are increasing (Figure 3b): the trapped continuum is observable in the [~0.4–3] kHz frequency range before the red-dashed line, and in the [~0.8–5] kHz frequency range between the red-dashed and black-dashed lines. This change in the cut-off frequencies is due to the inward motion of the magnetopause during the compression. Because of this, the local density along Juno's path is increasing, and therefore the low-frequency part of the trapped continuum cannot propagate, resulting in an increase in the cut-off frequencies of the trapped continuum. All these characteristics are the signature of the inward motion of the magnetopause boundary toward the spacecraft (see Figures 2c and 2f).

Furthermore, comparing the total amplitude of the magnetic field $|B|$ (blue curve) to Kivelson and Khurana (2002) and Khurana et al. (2004) magnetic field variation fit $|B_{\text{lobe}}|$, one can see that before ~18 December 2016 T09:00 (red dotted line), $|B|$ and $|B_{\text{lobe}}|$ follow the same trend. However, between ~18 December 2016 T09:00 and the

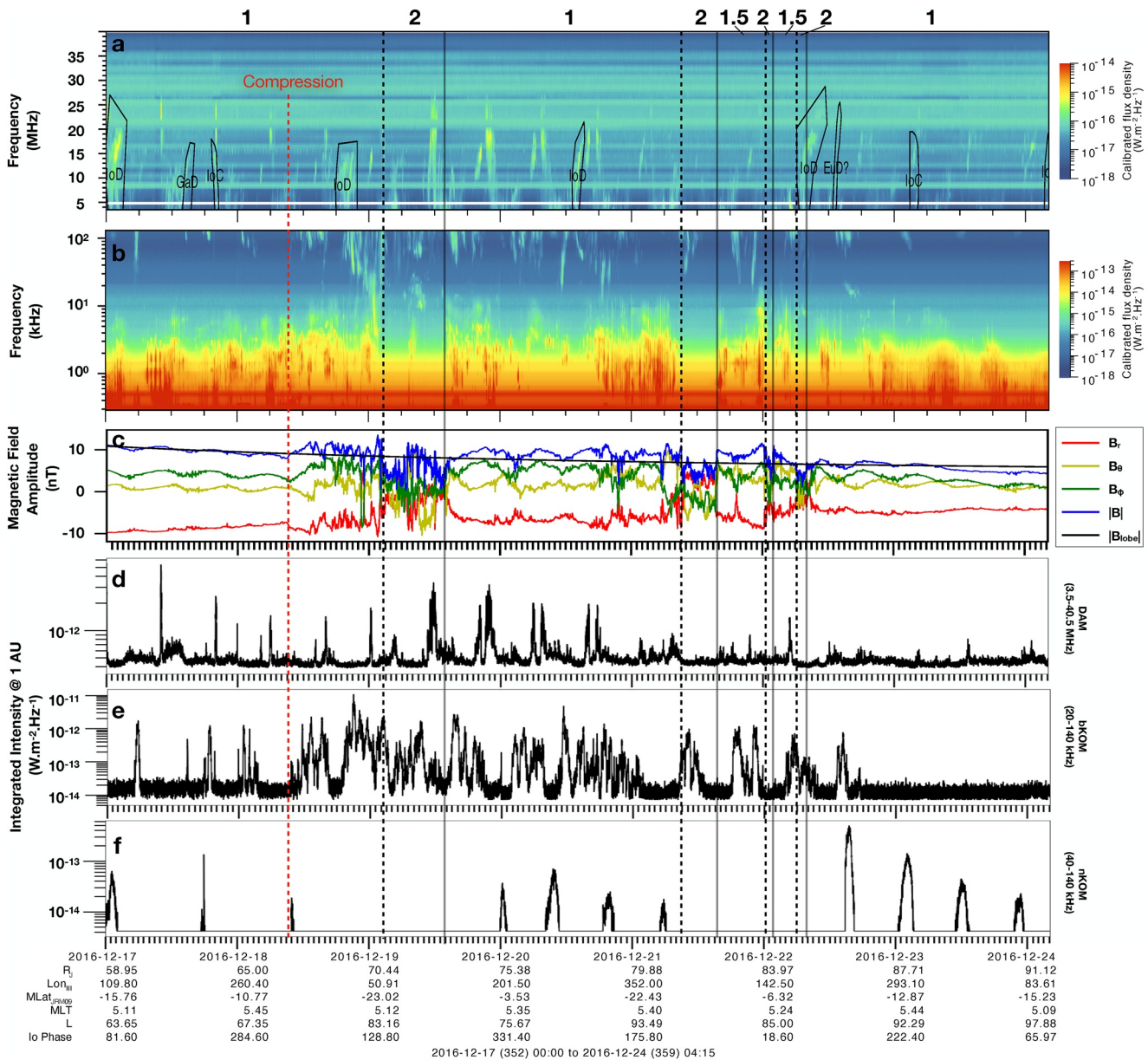


Figure 3. (a)–(c) Juno Waves and MAG measurements during a series of magnetopause crossings. Panels (a) and (b) show Juno Waves frequency-time spectrograms covering two different frequency ranges (from 3.5 to 40.5 MHz and between 3 and 140 kHz, respectively), with the black polygons in the top panel denoting the radio emissions induced by the interaction between Jupiter and its moons (e.g., Io, Europa, or Ganymede, based on Louis et al. (2021c)). Panel (c) shows the three components of magnetic field (in JSO spherical coordinates system, red, yellow, and green lines) and total field strength (blue). The black line displays the Kivelson and Khurana (2002) and Khurana et al. (2004) magnetic field variation fit. Panels (d)–(f) display time series of integrated flux density (normalized at 1 Astronomical Unit (AU), 15-s time resolution) for (d) the auroral decametric (DAM, in the 3.5–40.5 MHz range) not induced by the interaction between Jupiter and its moons (i.e., all the nonlabeled emissions), (e) broadband kilometric (bKOM, in the 20–140 kHz range), and (f) narrowband kilometric (nKOM, in the 40–140 kHz range) radio emissions. The black-dashed lines represent the outbound magnetopause crossings (from the magnetosphere to the magnetosheath) while the gray-shaded lines represent the inbound magnetopause crossings (from the magnetosheath to the magnetosphere). The red-dashed line represents the time when Juno starts to measure magnetic fluctuations and $|B| > |B_{lobe}|$ (panel c), and an increase in the low and high cut-off frequencies of the trapped continuum radiation (panel b). The numbers above the Waves data indicate the region where Juno is located: (1) magnetosphere, (2) magnetosheath, (1.5): “in” the magnetopause boundary.

crossing of the magnetopause (first black-dashed line), $|B|$ is above $|B_{lobe}|$, which is a clear sign that the magnetosphere is being compressed (see e.g., Jackman et al., 2010).

All these elements lead us to interpret this as representative of the beginning of the impact of a stronger solar wind on the magnetosphere, and thus the beginning of compression. On the other hand, after Juno crosses the

magnetopause for the second time (back into the magnetosphere, gray-shaded line) on ~19 December 2016 T14:12 and until the next outward crossing of the magnetopause (~21 December 2016 T08:48), we observe the same features: a variable low and high cut-off frequencies of the trapped continuum, small perturbations in the magnetic field components, and $|B| > |B_{lobe}|$. We interpret this as the relaxation phase of the magnetosphere, but not to a fully extended state. From the observations, we can deduce that Juno remains very close to the magnetopause (same characteristics as in Figures 2c and 2f), before the second compression takes place and the spacecraft is again in the magnetosheath.

By comparing the time spent by Juno inside the magnetosheath during the two compression events, we can infer whether one of the compressions was stronger than the other, i.e., lasted longer or the magnetopause was pushed further inwards. During the first pass from the magnetosphere to the magnetosheath, Juno stayed in it for ~12 hr 20 min, whereas during the second pass, Juno stayed inside the magnetosheath <7 hr, before going back into the magnetosphere very quickly twice for a few minutes. Therefore, we can deduce that the first compression either lasted longer or the magnetopause was pushed further inwards. In any case, we can infer that the magnetosphere was probably more disturbed by the first compression.

The Tao et al. (2005) solar wind propagation model is more reliable when Earth and Jupiter are in conjunction as seen from the Sun (Jupiter-Sun-Earth angle equal to 0°). During the time range displayed in Figure 3, the Jupiter-Sun-Earth angle is -110° (in average). Therefore, the error in timing on Tao et al. (2005) solar wind propagation model can be as large as 2 days or more, the time interval between the shocks can also be shifted, and P_{dyn} can be misjudged. Therefore, the outputs from the Tao et al. (2005) model should be used here only as a guide. For that reason, they are only displayed in the Supporting Information S1 (Figures S3 and S4), for information. According to Tao et al. (2005) model, two shocks arrive at Jupiter successively in a time interval of two and a half days. The model predicts the arrival of the first compression at the beginning of day 16 December 2016, i.e., 2 days before the first compression observed by Juno. By shifting the model outputs by 2 days (see Figure S4 in Supporting Information S1), we obtain a good match between the arrival of the two shocks at Jupiter and the compressions observed by Juno. These two shocks have very different characteristics (see Figure S3 in Supporting Information S1): (a) the first one shows an increase in the solar wind speed and a sharp decrease in the solar wind density and temperature, while (b) the second shock shows an increase in the solar wind speed, density, and temperature. Thus, if we take the outputs of Tao et al. (2005) model as reliable, the first shock would be an FRS while the second would be an FFS.

3.2. Response of the Auroral Radio Emission to the First Compression

Having determined the start time of the compression and the associated dynamic pressure, let us now study the response of the radio emissions to the first compression.

3.2.1. Broadband Kilometric (bKOM) Emission

The bKOM emissions (Figure 3e) are the first to show a strong variation. Before the onset of the compression, we can see some peaks in the integrated intensity, but restricted to a narrow frequency range (few 10s of kHz, see Figure 3b). Immediately after (dashed-red line at ~18 December 2016 T09:00), we observe emissions almost continuously, with an increase in the integrated intensity. This increase can be explained by both the observations of bKOM emissions over a much wider frequency range, i.e., from 20 to 140 kHz (see Figure 3b), and by the increase intensity of the emission. Very low-frequency extensions of the emission, i.e., emissions extended down to 20 kHz, are only visible over ~1 hr 15 min, thus only for specific sources. The bKOM emissions seen at almost every longitude are then observed until ~21 December 2016 T02:00, thus over >60 hr. The observation of emissions on an almost continuous basis tells us that sources have been activated at almost all longitudes. It should be noted that no bKOM emissions seem to be observed between 18 December 2016 T17:00 and 19:00. A sector of longitude therefore seems to have no associated bKOM emissions, at least during the first rotation. This could be due to various reasons, such as emissions that are too weak to be detected, geometric effects preventing the emission from being beamed toward the observer, or a sector that is completely nonactivated.

3.2.2. Decametric (DAM) Emission

After compression, an increase in the integrated intensity of the DAM radio emissions is also observed. However, unlike the bKOM emissions, this is not observed simultaneously with the onset of the magnetic disturbances,

nor is it continuous over time. DAM emissions visible before the compression (nonlabeled vertex early arc up to 15 MHz, see Figure 3a, statistically reported by Imai et al. (2017)) are still visible during the compression with the same rotation period, however their intensity has increased compared to before the compression. Therefore, the appearance of these emissions is probably modulated by rotation and independent of any compression. However, compression seems to have an impact on their intensity. New emissions, more intense and extending up to 25–30 MHz, appear at ~19 December 2016 T12:00, i.e., ~28 hr after the compression, and last for ~30 hr. Their rotation period is longer than the previously visible DAM emissions, visible with the double peak in the integrated time series Figure 3d, which means that the sources are subcorotating (see below).

Since the CMI emissions are not isotropically emitted, but only emitted at the edge of a hollow cone, with an angle of $\sim 75^\circ$ to $\sim 90^\circ$ with respect to the local magnetic field line (see Section 1), geometry effects are important, and emission is mostly seen by an observer when the sources are at a longitude $\sim 75^\circ$ – 90° greater or lower than the longitude of the observer. It can thus be complicated to disentangle between “no emission” and “nonvisible emission,” because the observer is not in the beam of the emission. For this, it can be interesting to have multipoint observations, e.g., including ground-based radio telescopes such as the NDA. Figure 4 displays observations taken by Juno (4a) and NDA (4b) on 19 December 2016. The observation geometry is shown in Figure 4c, with Juno located at a mean local time of 5.2 hr, and NDA at a mean local time of 12.64 hr, at the moment of the observations of the radio emissions. Finally, Figure 4d shows the shape of the radio emission as a function of the position of the sources relative to the observer.

Multiple “B” arcs are observed by Juno up to almost 30 MHz, between 11:00 and 12:30 (Figure 4a, see also Imai et al. (2017), who statistically reported these arcs). The type of the arcs and the position of Juno indicates that the emissions come from the midnight-to-dusk side as seen from Juno (see Figures 4c and 4d). On the other hand, between 09:00 and 09:30, “A” emissions are observed by the NDA (Figure 4b) up to almost 30 MHz. The type of the emissions seen by the NDA, and its position relative to Jupiter, indicates the emissions come from the dusk side as seen from Earth (see Figures 4c and 4d). By studying the time delay (e.g., at 24.5 MHz) between the first emission seen on 19 December 2016 T09:08 by the NDA (Earth Time, i.e., ~19 December 2016 T08:23 Juno Time, taking into account the light travel time) and the first emission seen on 19 December 2016 T12:27 (Juno Time) by Juno, we obtain a $\delta t = 4.1$ hr. According to the local time positions of the two observers, this is consistent with an emission originating from the same source, seen from both side of the beaming cone, and rotating with a subcorotation rate of $70 \pm 5\%$, meaning that the source is rotating at 70% of Jupiter's rotation angular frequency (taking into account that the emission at 24.5 MHz is beamed along a hollow cone with aperture angle of $75^\circ \pm 5^\circ$, Louis et al., 2017).

The beaming angle allowed by the CMI is in the range 75° – 90° , and Juno does not see a “B” radio emission before the NDA. Therefore, the onset region must be located in a region greater than Juno's local time plus 75° – 90° , and lower than NDA's local time minus 75° – 90° , therefore in the local time range $[1,110\text{--}1,740] \pm 0100$ hr.

The lack of emission observed by Juno is therefore partly due to geometry effects, but probably also to a delay in the activation of the sources and in a specific region (dusk). Indeed, the NDA sees an emission before Juno, but no emission is seen by Juno at the previous rotation, indicating that a time delay exists between the compression of the magnetosphere and the activation of newly activated DAM sources. This exact time delay is difficult to determine here, and would require a more statistical study or more observers, but it seems that at least two Jovian rotations are needed before new DAM sources are activated.

3.2.3. Narrowband Kilometric (nKOM) Emission

Finally, the delay for new nKOM emissions to be visible is far longer than for bKOM and DAM emissions. The first new emission appears at ~20 December 2016 T00:00, i.e., 39 hr after the first visible bKOM emission. The interval between the peaks in the integrated intensity is not regular, and varies between ~9 hr 14 min, ~10 hr 22 min, and ~9 hr 44 min. A closer look to the intensity peaks at different frequencies (see Figure S5b in Supporting Information S1) shows that the signal at lower frequencies (e.g., from 70.862 to 112.43 kHz) is triggered before the signal at higher frequencies (e.g., at 126.16 and 141.54 kHz), and then disappears first. The interval between the peaks seems to be different depending on the frequency, which implies different source locations (see Sections 3.3 and 4, for more details).

3.3. Response of the Auroral Radio Emission to the Second Compression

As mentioned at the beginning of this section, the dynamic pressure of the solar wind during the second compression event is potentially weaker than during the first event. This is suggested by both (a) the position of the

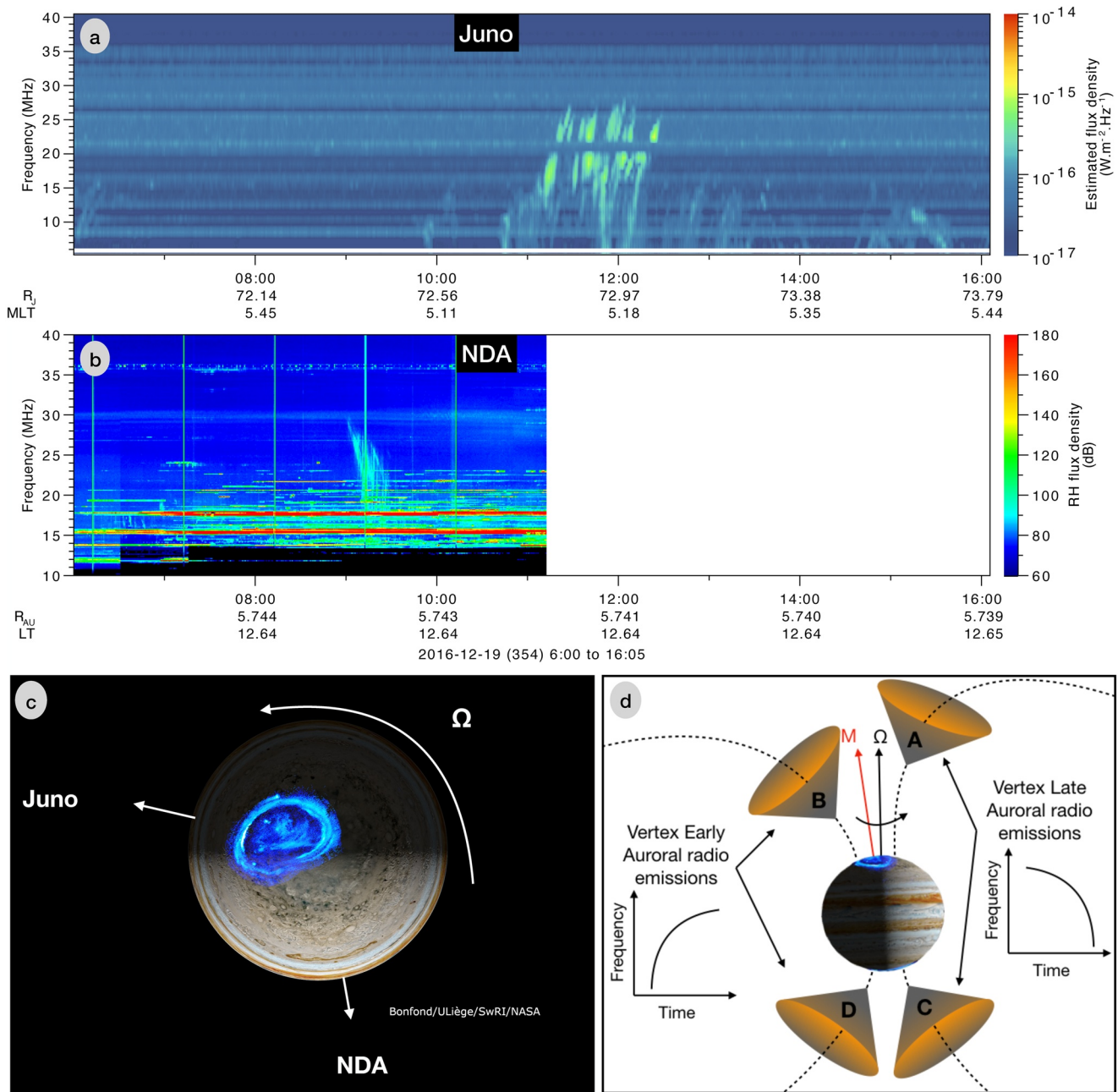


Figure 4. (a) Juno Waves and (b) Nançay Decameter Array (NDA) routine receiver observations. Decametric radio emissions are clearly visible (a) between 11:00 and 12:30 (Spacecraft Event Time) and (b) between 09:00 and 09:30 (UT time). The light travel time between Juno and Earth is ~ 47 min. The data gap after 11:10 is due to the fact that Jupiter is no longer visible in the sky from the NDA observatory. (c) Observers' configuration. (d) Cartoon of the geometry and nomenclature of the auroral radio emissions and corresponding arc shape in the (time, frequency) plane. If the source is located to the West of Jupiter for the observer (sources "B" or "D"), the emission will have a vertex early arc shape. If on the contrary the source is located to the East of Jupiter for the observer (sources "A" or "C"), the emission will have the shape of a vertex late arc. The arcs observed in panels (a) and (b) originate from the same source. NDA sees the emission cone exiting its field of view (vertex late arc) while Juno sees the emission cone entering its field of view (hence vertex early arc).

magnetopause, further away from Jupiter (see the second dotted black line at 21 December 2016 T08:48), and (b) the time spent in the magnetosphere which is shorter than during the first event.

The inspection of the radio emission time series shows that one DAM emission is observed at ~ 21 December 2016 T21:30, also observed one rotation later with greater intensity. This emission is most likely the reactivation of previously observed sources (as observed during the first compression event). Indeed DAM emission with

decreasing intensity is observed ~20 hr before (~21 December 2016 T01:30) with the same shape. Since the NDA is observing only one-third of the time we have no contemporaneous observations for this event.

New bKOM emission sources are activated at ~21 December 2016 T08:00. However, in contrast to the first event, fewer bKOM sources seem to have been activated, since the bKOM emission is not visible at all times, and the sources are activated for a shorter period of time (only visible for ~30 hr versus ~60 hr).

Finally, regarding the nKOM emission, new nKOM emissions are activated, starting at ~22 December 2016 T15:00, and lasting for ~40 hr (same duration as for the first compression), with integrated intensity higher than for the first event. This time, the delay between the activation of the bKOM and the nKOM emissions is only ~31 hr. Again, it can be seen that the period between the peaks in the integrated intensity is not regular. It varies between ~10 hr 30 min, ~9 hr 50 min, and ~10 hr 54 min. A closer look to the intensity peaks at different frequencies (see Figure S5c in Supporting Information S1) shows that the signal is first triggered at the lowest frequencies before being triggered at the highest frequencies. Then the signal disappears, or fades, in the same order. The interval between two peaks is different depending on the frequency. Focusing on distribution peaks at each frequency, it can be seen that periodicity increases with decreasing frequency. When the new nKOM emissions are activated, all peaks are almost centered at the same time (~22 December 2016 T15:45); one rotation later, the peaks are distributed in order of decreasing frequency, with the 141.54 kHz signal seen first and the 89.172 kHz signal peak seen last. This could be explained by the fact that the lower frequency nKOM is generated at lower density, hence, larger radial distances from Jupiter: the deviation from rigid corotation would be greater farther from the planet, and the periodicity should be longer.

4. Summary, Discussion, and Perspectives

In this paper, we have presented in Section 2 a set of magnetospheric boundary crossings (see Figure 1). More detailed information on each crossing, such as their exact time, their positions in different coordinate systems, and several added values (P_{dyn} , magnetopause and bow shock standoff distances) are given in Supporting Information S1 (Tables S1 and S2), as well as statistical distributions for these added values (Figure S2 in Supporting Information S1). The files corresponding to Tables S1 and S2 in Supporting Information S1 are accessible through Louis et al. (2022a).

In Section 3, we presented case studies of the response of Jovian radio emission to strong to moderate magnetospheric compressions, inferred by magnetopause crossings. Using the Joy et al. (2002) model, we calculated the dynamic pressure (lower limit) of the solar wind (see Table 1), and its main characteristics and type of shocks associated with these events using the Tao et al. (2005). We determined that the first magnetopause crossing is potentially due to (a) either a stronger and shorter compression, (b) or higher solar wind dynamic pressure, based on the time spent by Juno in the magnetosheath.

Table 1
Table Summarizing the Results of the Study of the Response Time of Radio Emissions to Compression, as Seen by Juno

Compression	P_{dyn}	Type of shock	Auroral radio emission	Activation time	Duration	
	(Joy et al., 2002)	(Tao et al., 2005)				
1st compression	0.70	FRS	bKOM	Main band	≤10s min	~60 hr
				LFE	~34 hr	1 hr 15 min
				DAM	~28 hr	~30 hr
				nKOM	~39 hr	~40 hr
2nd compression	0.48	FFS	bKOM	Main band	≤10 min	~30 hr
				LFE	≤10 min	~15 hr
				DAM	~12 hr 45 min	10 hr
				nKOM	~31 hr	~40 hr

Note. For each compression, the dynamic pressure of the solar wind (determined from the model of Joy et al. (2002)), the type of shock (determined from the model of Tao et al. (2005)), the response time of each component of the radio emission (main band of the bKOM, low-frequency extension (LFE) of the bKOM, DAM, and nKOM) and the activation time (as seen by Juno) are given.

We chose to study the magnetopause crossings occurring between 17 December 2016 T00:00 and 24 December 2016 T04:15 (fourth orbit of Juno). These magnetopause crossings are among the innermost cases (see Figure 1a and Figure S1a in Supporting Information S1), corresponding to strong compressions ($P_{\text{dyn}} \subset [0.5\text{--}0.7]$) according to the Joy et al. (2002) model). These compressions occur when Juno is still on the dawn side of the magnetosphere, i.e., in a region where the model of Joy et al. (2002) is valid, in contrast to the dusk side where it is less constrained. Moreover, during this 7-day interval, we observe several magnetopause crossings, which can be grouped into two phases of magnetospheric compression. These two cases also seem to correspond to two different types of shocks: FFS and FRS, according to the propagation model of Tao et al. (2005), with different responses observed in the radio components (see Table 1).

Concerning the radio emission response to the compressions, we have determined that the bKOM sources are the first to be triggered, at almost every longitude, almost immediately after the observation of the first magnetic disturbances and density perturbations. The bKOM emission is then observed over 60 hr for the first compression and for 30 hr for the second one. Low-frequency extensions, i.e., emissions going down to 20 kHz, are observed in both cases for a shorter duration.

In both cases, the DAM emissions are the second ones to be observed, at least one rotation after the start of the compression, and only in the noon-dusk sector, i.e., inside the local time range [1,110–1,740]. This sector includes that determined by Hess et al. (2012, 2014), but is necessarily less precise given that we are only studying two cases here. A statistical study with Juno will provide further constraints, given the evolution of Juno's local time position during its mission. Our results seem to show that both FRS and FFS activate new, or reactivate, DAM emissions on the dusk side only. This is partially in agreement with Hess et al. (2012, 2014) who showed that FFS mainly trigger DAM emission on the dusk side, while FRS trigger emissions on the dusk and dawn sides. However, since we are measuring radio emission only above 3.5 MHz in this study (due to Waves sensitivity) we are missing part of the DAM and most of the HOM emissions, that can go down to 0.3 MHz, while Hess et al. (2012, 2014) used Cassini radio measurements, down to 0.1 MHz. The DAM emission lasts for 30 hr in the first case, and 10 hr in the second case. In both cases, sources rotate in subcorotation, with a rate of $70 \pm 5\%$ of rigid corotation. This value is comparable with the values obtained by Hess et al. (2012, 2014).

Concerning the activated nKOM emissions, we observe a strong difference compared to the bKOM and DAM emissions, with a long delay between compression and activation of the nKOM sources ($\sim 30\text{--}40$ hr). nKOM emission is then observed for ~ 40 hr in both compression events. The periodicity of the nKOM peaks is frequency-dependent and increases with decreasing frequency. This would be related to the mechanism, producing emissions at the plasma frequency which is proportional to the local plasma density. Therefore, low-frequency emissions are produced farther from Jupiter than higher-frequency emissions. The activation of new nKOM sources seems related to the relaxation/reconfiguration phase of the magnetosphere. As these emissions are produced by different mechanisms, it is not surprising that the activation of these emissions is also different. However, it is possible that the energetic events observed by Louarn et al. (1998, 2016) could be caused or amplified by an expansion of the magnetosphere, which would amplify the centrifugal ejection of matter. It will therefore be mandatory to study in detail the nKOM during plasma sheet distortion, which will require a list of magnetic disturbances measured during plasma sheet crossings, simultaneously to compression events. But this is beyond the scope of this current article, and will be the subject of an upcoming study.

To get a better estimate of the conditions in the solar wind, such as the solar wind dynamic pressure and velocity, the Thomsen et al. (2019) analytical method could be used, based on Juno/JADE measurements inside the magnetosheath (Juno/JADE data were not available for the event studied in Section 3). This will be compared to estimation of the dynamic pressure obtained from Joy et al. (2002) magnetosphere boundaries model and Tao et al. (2005) propagation tool model. We could also use different solar wind propagation tools, such as “HuXT” model (Heliospheric Upwind Extrapolation with time dependence; Owens et al., 2020), “WSA-ENLIL solar wind simulation,” “HelioCast” (Réville et al., 2023), or the “CDPP/Propagation Tool” extended to Jupiter (Rouillard et al., 2017).

To go further on the generalization of the response of Jovian radio emissions, the activation of new sources or the amplification of existing radio emissions, and their intensity to magnetospheric compression and solar wind characteristics (dynamic pressure, velocity, temperature, magnetic field orientation), a statistical study will be necessary. The same method will be used and will be applied to all the compression events determined from the list of magnetopause crossings provided in the Supporting Information S1 tables (see also Figures 1 and Figure

S1 in Supporting Information S1). This will involve using boundary crossings to infer compressions, examining the response of associated radio emissions, and grouping case studies by properties such as solar wind dynamic pressure, or shock type.

There are several benefits to a future statistical study. The first is to explore the differences between dawn and dusk side responses, and the different properties of the boundaries of the magnetosphere (e.g., Kelvin-Helmholtz instability, Michael et al., 2021), or the differences in the observation of radio sources (beaming constraints). The second aspect is the opportunity to explore different classes of behavior in terms of magnetospheric compression state. Due to the precession of the apojoves, we observe the compression of the magnetosphere from different positions in the magnetosphere. As shown in Figure 1c, the nature of the boundary motion is highly variable, and the number of boundary crossings varies greatly from one orbit to another. Some orbits have clean boundary crossings, while other orbits have multiple crossings in a short time. This makes it possible to study the radio response during the compression and relaxation phases, but also during the stationary state—see Figures 2c and 2f for an example. Third, the long period of time between Juno's insertion into Jovian orbit (July 2016) and the latest orbits of the extended mission (perijoves ≥ 50) covers two different phases of two different solar cycles and different Jovian seasons, which could allow us to explore the response of radio emissions to compression as a function of the solar cycles and Jovian seasons.

At the time of writing, Juno is still crossing the boundaries on the high southern latitude dusk side, and thus a full statistical exploration of the broad parameter space should await the completion of these apojove passes. Moreover, the comprehensive labeled radio emissions catalog (Louis et al., 2021c) is currently being updated to cover the whole mission.

Data Availability Statement

The Juno/Waves data set displayed in this paper, produced by Louis et al. (2021a), is accessible at <https://doi.org/10.25935/6jg4-mk86> (Louis et al., 2021b), and the catalogue can be download at <https://doi.org/10.25935/nhb2-wy29> (Louis et al., 2021c). The Juno/MAG magnetic field data are accessible through the NASA/PDS website (Connerney, 2017). Figure 1 was produced using the Jupiter magnetosphere boundaries crossings given in the Tables S1 and S2 in Supporting Information S1 (Louis et al., 2022a). Juno/Waves and Juno/MAG data were displayed using the Autoplot tool (Faden et al., 2010). The NDA data set displayed in Figure 4 is accessible at <https://doi.org/10.25935/PBPE-BF82> (Lamy et al., 2021). The routine that allows to determine the dynamic pressure from the Joy et al. (2002) model are accessible at https://github.com/DIASPlanetary/jupiter_magnetosphere_boundaries. Juno ephemeris and MAG data (in JSO coordinates system) were retrieved from <http://amda.cdpp.eu/> (Génot et al., 2021). Juno ephemeris used to infer the dynamic pressure (in JSS coordinate) were retrieved from <https://wgc.jpl.nasa.gov:8443/webgeocalc/#StateVector>.

Acknowledgments

C. K. Louis', C. M. Jackman's, A. R. Fogg's, and S. C. McEntee's work at the Dublin Institute for Advanced Studies was funded by the Science Foundation Ireland Grant 18/FRL/6199. D. M. Weigt's work at the Dublin Institute for Advanced Studies was funded by the European Union's Horizon 2020 research and innovation programme under Grant Agreement 952439 and project number AO 2-1927/22/NL/GLC/ov as part of the ESA OSIP Nanosats for Spaceweather Campaign D. M. Weigt's work at Aalto University was funded from the European Research Council (ERC) under the European Union's Horizon 2020 research and innovation programme (project "SYCOS," Grant Agreement 101101005). The research at the University of Iowa was supported by NASA through Contract 699041X with the Southwest Research Institute. W. S. Kurth acknowledges the use of the Space Physics Data Repository at the University of Iowa supported by the Roy J. Carver Charitable Trust.

References

- Barbosa, D. D. (1982). Low-level VLF and LR radio emissions observed at earth and Jupiter. *Reviews of Geophysics and Space Physics*, 20(2), 316–334. <https://doi.org/10.1029/RG020i002p00316>
- Cecconi, B., Witasse, O., Jackman, C. M., Sánchez-Cano, B., & Mays, M. L. (2022). Effect of an interplanetary coronal mass ejection on Saturn's radio emission. *Frontiers in Astronomy and Space Sciences*, 9, 800279. <https://doi.org/10.3389/fspas.2022.800279>
- Collier, M. R., Gruesbeck, J. R., Connerney, J. E. P., Joy, S. P., Hospodarsky, G. B., Roberts, A., et al. (2020). A K-means clustering analysis of the Jovian and terrestrial magnetopauses: A technique to classify global magnetospheric behavior. *Journal of Geophysical Research: Planets*, 125, e2019JE006366. <https://doi.org/10.1029/2019JE006366>
- Connerney, J. E. P. (2017). Juno MAG CALIBRATED DATA J V1.0, JNO-J-3-FGM-CAL-V1.0 [Dataset]. <https://doi.org/10.17189/1519711>
- Connerney, J. E. P., Bann, M., Bjarne, J. B., Denver, T., Espley, J., Jorgensen, J. L., et al. (2017). The Juno magnetic field investigation. *Space Science Reviews*, 213(1–4), 39–138. <https://doi.org/10.1007/s11214-017-0334-z>
- Echer, E., Zarka, P., Gonzalez, W. D., Morioka, A., & Denis, L. (2010). Solar wind effects on Jupiter non-Io DAM emissions during Ulysses distant encounter (2003-2004). *Astronomy & Astrophysics*, 519, A84. <https://doi.org/10.1051/0004-6361/200913305>
- Faden, J. B., Weigel, R. S., Merka, J., & Friedel, R. H. W. (2010). Autoplot: A browser for scientific data on the web. *Earth Science Informatics*, 3(1–2), 41–49. <https://doi.org/10.1007/s12145-010-0049-0>
- Filbert, P. C., & Kellogg, P. J. (1979). Electrostatic noise at the plasma frequency beyond the earth's bow shock. *Journal of Geophysical Research*, 84(A4), 1369–1381. <https://doi.org/10.1029/JA084iA04p01369>
- Fogg, A. R., Jackman, C. M., Waters, J. E., Bonnin, X., Lamy, L., Cecconi, B., et al. (2022). Wind/Waves observations of auroral kilometeric radiation: Automated burst detection and terrestrial solar wind-magnetosphere coupling effects. *Journal of Geophysical Research: Space Physics*, 127, e2021JA030209. <https://doi.org/10.1029/2021JA030209>
- Génot, V., Budnik, E., Jacquey, C., Bouchemit, M., Renard, B., Dufour, N., et al. (2021). Automated Multi-Dataset Analysis (AMDA): An on-line database and analysis tool for heliospheric and planetary plasma data. *Planetary and Space Sciences*, 201, 105214. <https://doi.org/10.1016/j.pss.2021.105214>

- Genova, F., Zarka, P., & Barrow, C. H. (1987). Voyager and Nancay observations of the Jovian radio-emission at different frequencies-solar wind effect and source extent. *Astronomy & Astrophysics*, *182*, 159–162.
- Gurnett, D. A., Kurth, W. S., Hospodarsky, G. B., Persoon, A. M., Zarka, P., Lecacheux, A., et al. (2002). Control of Jupiter's radio emission and aurorae by the solar wind. *Nature*, *415*(6875), 985–987. <https://doi.org/10.1038/415985a>
- Gurnett, D. A., & Scarf, F. L. (1983). *Physics of the Jovian magnetosphere* (pp. 285–316). Cambridge University Press.
- Hess, S. L. G., Echer, E., & Zarka, P. (2012). Solar wind pressure effects on Jupiter decametric radio emissions independent of Io. *Planetary and Space Science*, *70*(1), 114–125. <https://doi.org/10.1016/j.pss.2012.05.011>
- Hess, S. L. G., Echer, E., Zarka, P., Lamy, L., & Delamere, P. A. (2014). Multi-instrument study of the Jovian radio emissions triggered by solar wind shocks and inferred magnetospheric subcorotation rates. *Planetary and Space Science*, *99*, 136–148. <https://doi.org/10.1016/j.pss.2014.05.015>
- Hospodarsky, G. B., Kurth, W. S., Bolton, S. J., Allegrini, F., Clark, G. B., Connerney, J. E. P., et al. (2017). Jovian bow shock and magnetopause encounters by the Juno spacecraft. *Geophysical Research Letters*, *44*, 4506–4512. <https://doi.org/10.1002/2017GL073177>
- Imai, M., Greathouse, T. K., Kurth, W. S., Gladstone, G. R., Louis, C. K., Zarka, P., et al. (2019). Probing Jovian broadband kilometric radio sources tied to the ultraviolet main auroral oval with Juno. *Geophysical Research Letters*, *46*, 571–579. <https://doi.org/10.1029/2018GL081227>
- Imai, M., Imai, K., Higgins, C. A., & Thieman, J. R. (2008). Angular beaming model of Jupiter's decametric radio emissions based on Cassini RPWS data analysis. *Geophysical Research Letters*, *35*, L17103. <https://doi.org/10.1029/2008GL034987>
- Imai, M., Imai, K., Higgins, C. A., & Thieman, J. R. (2011). Comparison between Cassini and Voyager observations of Jupiter's decametric and hectometric radio emissions. *Journal of Geophysical Research*, *116*, A12233. <https://doi.org/10.1029/2011JA016456>
- Imai, M., Kurth, W. S., Hospodarsky, G. B., Bolton, S. J., Connerney, J. E. P., & Levin, S. M. (2017). Statistical study of latitudinal beaming of Jupiter's decametric radio emissions using Juno. *Geophysical Research Letters*, *44*, 4584–4590. <https://doi.org/10.1002/2017GL073148>
- Jackman, C. M., & Arridge, C. S. (2011). Solar cycle effects on the dynamics of Jupiter's and Saturn's magnetospheres. *Solar Physics*, *274*(1–2), 481–502. <https://doi.org/10.1007/s11207-011-9748-z>
- Jackman, C. M., Arridge, C. S., Slavin, J. A., Milan, S. E., Lamy, L., Dougherty, M. K., & Coates, A. J. (2010). In situ observations of the effect of a solar wind compression on Saturn's magnetotail. *Journal of Geophysical Research*, *115*, A10240. <https://doi.org/10.1029/2010JA015312>
- Jones, D. (1988). Planetary radio emissions from low magnetic latitudes—observations and theories. In *Planetary radio emissions II* (pp. 245–281). Joy, S. P., Kivelson, M. G., Walker, R. J., Khurana, K. K., Russell, C. T., & Ogino, T. (2002). Probabilistic models of the Jovian magnetopause and bow shock locations. *Journal of Geophysical Research*, *107*(A10), 1309. <https://doi.org/10.1029/2001JA009146>
- Khurana, K. K., Kivelson, M. G., Vasylunas, V. M., Krupp, N., Woch, J., Lagg, A., et al. (2004). The configuration of Jupiter's magnetosphere. In F. Bagenal, T. E. Dowling, & W. B. McKinnon (Eds.), *Jupiter: the planet, satellites and magnetosphere* (Vol. 1, pp. 593–616).
- Kilpua, E. K. J., Lumme, E., Andreoeva, K., Isavnin, A., & Koskinen, H. E. J. (2015). Properties and drivers of fast interplanetary shocks near the orbit of the earth (1995–2013). *Journal of Geophysical Research: Space Physics*, *120*, 4112–4125. <https://doi.org/10.1002/2015JA021138>
- Kivelson, M. G., & Khurana, K. K. (2002). Properties of the magnetic field in the Jovian magnetotail. *Journal of Geophysical Research*, *107*(A8), 1196. <https://doi.org/10.1029/2001JA000249>
- Kurth, W. S., Hospodarsky, G. B., Kirchner, D. L., Mokrzycki, B. T., Averkamp, T. F., Robison, W. T., et al. (2017). The Juno waves investigation. *Space Science Reviews*, *213*(1–4), 347–392. <https://doi.org/10.1007/s11214-017-0396-y>
- Ladreiter, H. P., Zarka, P., & Lacacheux, A. (1994). Direction finding study of Jovian hectometric and broadband kilometric radio emissions: Evidence for their auroral origin. *Planetary and Space Science*, *42*(11), 919–931. [https://doi.org/10.1016/0032-0633\(94\)90052-3](https://doi.org/10.1016/0032-0633(94)90052-3)
- Lamy, L., Kenfack, G., Zarka, P., Cecconi, B., Viou, C., Renaud, P., et al. (2021). Nançay Decameter Array (NDA) Jupiter Juno-Nançay data collection (Version 1.0) [Dataset]. PADC/MASER. <https://doi.org/10.25935/PBPE-BF82>
- Louarn, P., Allegrini, F., McComas, D. J., Valek, P. W., Kurth, W. S., André, N., et al. (2017). Generation of the Jovian hectometric radiation: First lessons from Juno. *Geophysical Research Letters*, *44*, 4439–4446. <https://doi.org/10.1002/2017GL072923>
- Louarn, P., Allegrini, F., McComas, D. J., Valek, P. W., Kurth, W. S., André, N., et al. (2018). Observation of electron conics by Juno: Implications for radio generation and acceleration processes. *Geophysical Research Letters*, *45*, 9408–9416. <https://doi.org/10.1029/2018GL078973>
- Louarn, P., Kivelson, M. G., & Kurth, W. S. (2016). On the links between the radio flux and magnetodisk distortions at Jupiter. *Journal of Geophysical Research: Space Physics*, *121*, 9651–9670. <https://doi.org/10.1002/2016JA023106>
- Louarn, P., Roux, A., Perraut, S., Kurth, W., & Gurnett, D. (1998). A study of the large-scale dynamics of the Jovian magnetosphere using the Galileo Plasma Wave Experiment. *Geophysical Research Letters*, *25*(15), 2905–2908. <https://doi.org/10.1029/98GL01774>
- Louis, C. K., Jackman, C., Mangham, S., Smith, K., O'Dwyer, E., Empey, A., et al. (2022b). The “SPectrogram Analysis and Cataloguing Environment” (SPACE) labelling tool. *Frontiers in Astronomy and Space Sciences*, *9*, 1001166. <https://doi.org/10.3389/fspas.2022.1001166>
- Louis, C. K., Cecconi, B., & Loh, A. (2020). EXPRES Jovian radio emission simulations data collection (version 01). PADC. <https://doi.org/10.25935/KPGE-ZB59>
- Louis, C. K., Hess, S. L. G., Cecconi, B., Zarka, P., Lamy, L., Aicardi, S., & Loh, A. (2019b). EXPRES: An exoplanetary and planetary radio emissions simulator. *Astronomy & Astrophysics*, *627*, A30. <https://doi.org/10.1051/0004-6361/201935161>
- Louis, C. K., Hospodarsky, G., Jackman, C. M., O'Kane Hackett, A., Devon-Hurley, E., Kurth, W. S., et al. (2022a). Lists of magnetopause and bow shock crossings, as measured by Juno/Waves and Juno/MAG (1.0.0) [Dataset]. DIAS/Zenodo. <https://doi.org/10.5281/zenodo.7304517>
- Louis, C. K., Jackman, C. M., Mangham, S. W., Smith, K. D., O'Dwyer, E., Empey, A., et al. (2022c). SPACE labelling tool version 2.0.0 (v2.0.0) [Code]. Zenodo. <https://doi.org/10.5281/zenodo.6886528>
- Louis, C. K., Lamy, L., Zarka, P., Cecconi, B., Imai, M., Kurth, W. S., et al. (2017). Io-Jupiter decametric arcs observed by Juno/Waves compared to EXPRES simulations. *Geophysical Research Letters*, *44*, 9225–9232. <https://doi.org/10.1002/2017GL073036>
- Louis, C. K., Prangé, R., Lamy, L., Zarka, P., Imai, M., Kurth, W. S., & Connerney, J. E. P. (2019a). Jovian auroral radio sources detected in situ by Juno/Waves: Comparisons with model auroral ovals and simultaneous HST FUV images. *Geophysical Research Letters*, *46*, 11606–11614. <https://doi.org/10.1029/2019GL084799>
- Louis, C. K., Zarka, P., & Cecconi, B. (2021b). Juno/Waves estimated flux density Collection (Version 1.0). PADC/MASER. <https://doi.org/10.25935/6jg4-mk86>
- Louis, C. K., Zarka, P., Cecconi, B., & Kurth, W. S. (2021c). Catalogue of Jupiter radio emissions identified in the Juno/Waves observations (Version 1.0). PADC/MASER. <https://doi.org/10.25935/nhb2-wy29>
- Louis, C. K., Zarka, P., Dabidin, K., Lampson, P. A., Magalhães, F. P., Boudouma, A., et al. (2021a). Latitudinal beaming of Jupiter's radio emissions from Juno/Waves flux density measurements. *Journal of Geophysical Research: Space Physics*, *126*, e2021JA029435. <https://doi.org/10.1029/2021JA029435>
- Mauk, B. H., Mitchell, D. G., McEntire, R. W., Paranicas, C. P., Roelof, E. C., Williams, D. J., & Lagg, A. (2004). Energetic ion characteristics and neutral gas interactions in Jupiter's magnetosphere. *Journal of Geophysical Research*, *109*, A09S12. <https://doi.org/10.1029/2003JA010270>

- McComas, D. J., Alexander, N., Allegrini, F., Bagenal, F., Beebe, C., Clark, G., et al. (2017). The Jovian Auroral Distributions Experiment (JADE) on the Juno mission to Jupiter. *Space Science Reviews*, 213(1–4), 547–643. <https://doi.org/10.1007/s11214-013-9990-9>
- Michael, A. T., Sorathia, K. A., Merkin, V. G., Nykyri, K., Burkholder, B., Ma, X., et al. (2021). Modeling Kelvin-Helmholtz instability at the high-latitude boundary layer in a global magnetosphere simulation. *Geophysical Research Letters*, 48, e2021GL094002. <https://doi.org/10.1029/2021GL094002>
- Montgomery, J., Ebert, R. W., Clark, G., Fuselier, S. A., Allegrini, F., Bagenal, F., et al. (2022). Investigating the occurrence of magnetic reconnection at Jupiter's dawn magnetopause during the Juno Era. *Geophysical Research Letters*, 49, e2022GL099141. <https://doi.org/10.1029/2022GL099141>
- Owens, M., Lang, M., Barnard, L., Riley, P., Ben-Nun, M., Scott, C. J., et al. (2020). A computationally efficient, time-dependent model of the solar wind for use as a surrogate to three-dimensional numerical magnetohydrodynamic simulations. *Solar Physics*, 295(3), 43. <https://doi.org/10.1007/s11207-020-01605-3>
- Ranquist, D. A., Bagenal, F., Wilson, R. J., Hospodarsky, G., Ebert, R. W., Allegrini, F., et al. (2019). Survey of Jupiter's dawn magnetosheath using Juno. *Journal of Geophysical Research: Space Physics*, 124, 9106–9123. <https://doi.org/10.1029/2019JA027382>
- Réville, V., Poirier, N., Kouloumvakos, A., Rouillard, A. P., Ferreira Pinto, R., Fargette, N., et al. (2023). HelioCast: Heliospheric forecasting based on white-light observations of the solar corona. *Journal of Space Weather and Space Climate*, 13, 11. <https://doi.org/10.1051/swsc/2023008>
- Ronnmark, K. (1992). Conversion of Upper Hybrid waves into magnetospheric radiation. In *Planetary radio emissions III* (pp. 405–417).
- Rouillard, A. P., Lavraud, B., Génot, V., Bouchemit, M., Dufourg, N., Plotnikov, I., et al. (2017). A propagation tool to connect remote-sensing observations with in-situ measurements of heliospheric structures. *Planetary and Space Science*, 147, 61–77. <https://doi.org/10.1016/j.pss.2017.07.001>
- Scarf, F. L., Fredricks, R. W., Frank, L. A., & Neugebauer, M. (1971). Nonthermal electrons and high-frequency waves in the upstream solar wind, 1. Observations. *Journal of Geophysical Research*, 76(22), 5162–5171. <https://doi.org/10.1029/JA076i022p05162>
- Smith, E. J., & Wolfe, J. H. (1976). Observations of interaction regions and corotating shocks between one and five AU: Pioneers 10 and 11. *Geophysical Research Letters*, 3(3), 137–140. <https://doi.org/10.1029/GL003i003p00137>
- Tao, C., Kataoka, R., Fukunishi, H., Takahashi, Y., & Yokoyama, T. (2005). Magnetic field variations in the Jovian magnetotail induced by solar wind dynamic pressure enhancements. *Journal of Geophysical Research*, 110, A11208. <https://doi.org/10.1029/2004JA010959>
- Thomsen, M. F., Jackman, C. M., & Lamy, L. (2019). Solar wind dynamic pressure upstream from Saturn: Estimation from magnetosheath properties and comparison with SKR. *Journal of Geophysical Research: Space Physics*, 124, 7799–7819. <https://doi.org/10.1029/2019JA026819>
- Treumann, R. A. (2006). The electron-cyclotron maser for astrophysical application. *Astronomy & Astrophysics*, 13(4), 229–315. <https://doi.org/10.1007/s00159-006-0001-y>
- Tsurutani, B. T., Gonzalez, W. D., Gonzalez, A. L. C., Guarnieri, F. L., Gopalswamy, N., Grande, M., et al. (2006). Corotating solar wind streams and recurrent geomagnetic activity: A review. *Journal of Geophysical Research*, 111, A07S01. <https://doi.org/10.1029/2005JA011273>
- Went, D. R., Kivelson, M. G., Achilleos, N., Arridge, C. S., & Dougherty, M. K. (2011). Outer magnetospheric structure: Jupiter and Saturn compared. *Journal of Geophysical Research*, 116, A04224. <https://doi.org/10.1029/2010JA016045>
- Zarka, P. (1998). Auroral radio emissions at the outer planets: Observations and theories. *Journal of Geophysical Research*, 103(E9), 20159–20194. <https://doi.org/10.1029/98JE01323>
- Zarka, P., & Genova, F. (1983). Low-frequency Jovian emission and solar wind magnetic sector structure. *Nature*, 306(5945), 767–768. <https://doi.org/10.1038/306767a0>
- Zarka, P., Magalhães, F. P., Marques, M. S., Louis, C. K., Echer, E., Lamy, L., et al. (2021). Jupiter's auroral radio emissions observed by Cassini: Rotational versus solar wind control, and components identification. *Journal of Geophysical Research: Space Physics*, 126, e2021JA029780. <https://doi.org/10.1029/2021JA029780>